

Simulation and Prediction of Countercurrent Spontaneous Imbibition at Early and Late Times Using Physics-Informed Neural Networks

Jassem Abbasi*, Pål Østebø Andersen
Department of Energy Resources, University of Stavanger, Norway
* jassem.abbasi@uis.no

Abstract

Countercurrent spontaneous imbibition (COUCSI) is a process in porous materials in which a wetting phase displaces non-wetting phase. In this work, we investigate for the first time the application of Physics-Informed Neural Networks (PINNs) in solving the 1D COUCSI problem in both early (ET) and late (LT) times (before and after the imbibition front meets the no-flow boundary). Also novel, we examine the Change-of-Variables technique for improving the performance of PINNs. We formulated the COUCSI problem in three equivalent forms by changing the independent variables: XT-, XY-, and Z-formulations. The first describes saturation as function of normalized position X and time T; the second as function of X and $Y=T^{0.5}$; and the third as a sole function of $Z=X/T^{0.5}$ (valid only at ET). The PINN model was generated using a feed-forward neural network and trained based on minimizing a weighted loss function, including the physics-informed loss term and terms corresponding to the initial and boundary conditions. No synthetic or experimental data were involved in the training. The generalization ability was tested by applying the workflow to two imbibition cases with different displacement profile behavior. All three formulations could closely approximate the correct solutions (obtained by fine-grid numerical simulations), with water saturation mean absolute errors (MAE) around 0.019 and 0.009 for XT and XY formulations and 0.012 for the Z formulation at ET. The Z formulation perfectly captured the self-similarity of the system at ET. This was less captured by XT and XY formulations. The total variation (TV) of saturation was preserved in the Z formulation, and it was better preserved with XY- than XT formulation. It was demonstrated that redefining the problem based on physics-inspired variables reduced the non-linearity of the problem and allowed higher solution accuracies, a higher degree of loss-landscape convexity, a lower number of required collocation points, smaller network sizes, and more computationally efficient solutions.

Keywords: Spontaneous Imbibition; Physics Informed Neural Networks; Partial Differential Equations, Change of Variables

Introduction

Spontaneous imbibition (SI) is a flow phenomenon where a wetting phase diffuses into porous media and displaces a non-wetting phase due to capillary forces. This process commonly occurs in geological problems, such as soil water infiltration, hydrocarbon production, and carbon sequestration. Analyzing the spontaneous imbibition process provides insights into the wetting condition of the system (if the surrounding fluid wets the porous system) and the governing capillary pressure curve regarding how strong capillary forces are present and how much fluid displacement they can cause (Mason & Morrow, 2013). The boundary conditions influence the flow behavior during SI. In systems where both fluids access the system through the same surface, they flow counter-currently. This is called countercurrent SI (COUCSI). When some system surfaces are exposed to the wetting phase and other surfaces to non-wetting phase, the fluids predominantly flow in the same direction, which is called co-current SI (COCSI) (Bourbiaux & Kalaydjian, 1990).

During COUCSI, we distinguish between the early time (ET) period (when the invading saturation profile has not reached the closed boundary) and the late time (LT) period (when the no-flow boundary

has been reached). In ET, the advancement of the front is proportional to the square root of time (Y. Li et al., 2006), and there is a self-similarity behavior in the saturation front of fluid versus a similarity variable (Barenblatt et al., 1990; Y. Li et al., 2003). The recovery stays proportional to the square root of time during ET. However, it has been demonstrated comprehensively that recovery can follow this trend long into the LT regime (Andersen, 2021, 2023b; March et al., 2016). The explanation is that the imbibition rate at the inlet, which controls recovery, acts as if it is still ET until the saturation profile has changed sufficiently from the self-similar ET saturation profile at the inlet (Andersen, 2023a).

The 1D COUCSI problem can be solved numerically with finite differences (FD) approaches using, e.g., reservoir simulators (Abbasi & Andersen, 2022; Khan et al., 2018). Analytical solutions can be derived for very specific saturation functions or piston-like displacement (Cil & Reis, 1996; Fokas & Yortsos, 1982; Kashchiev & Firoozabadi, 2003). Semi-analytical solutions were derived by McWhorter & Sunada (1990) that hold for any input parameters and saturation functions, except being limited to ET. Bjørnarå & Mathias (2013) noted numerical challenges in evaluating their solution and proposed more stable schemes. Numerical approaches are usually required for more complex problems involving more general geometries or changing boundary conditions. Schmid & Geiger (2012) used McWhorter and Sunada's solution to propose a universal time scale for COUCSI. Andersen (2023b) showed that all 1D COUCSI problems (regardless of wettability, saturation functions, and other parameters) could be normalized to the same form, which only depends on a normalized diffusion coefficient with a mean equal to one. By correlating the coefficient shape with recovery behavior, ET and LT recovery were predicted accurately without the need for numerical methods.

Physics-informed neural networks (PINNs) provide an alternative approach to solving ordinary- and partial- differential equations (ODEs and PDEs) that govern various engineering problems (Karniadakis et al., 2021). PINNs have recently been applied to mathematical analysis of flow in porous media: Fraces & Tchelepi (2021), Almajid & Abu-Al-Saud (2022), and Rodriguez-Torrado et al. (2022) utilized PINNs for solving the Buckley-Leverett (BL) equation describing the displacement of oil by water flooding. A key challenge was capturing the shock front behavior. Deng & Pan (2021) applied PINN to study 1D spontaneous imbibition using Lagrangian formulation. They investigated ET flow for self-similar counter- and co-current flow and also considered more general boundary conditions during co-current SI where the ET flow would not be self-similar due to countercurrent production at the inlet. In the self-similar system, they could determine the saturation-dependent characteristic flow function, fluxes as a function of time, and solutions of saturation along the core. The sensitivity of problem formulation of COUCSI to capture self-similarity and other properties has not been explored. To our knowledge, the current work is only the second study investigating PINN applied to (COUC)SI. A problem's non-linearity may reduce the accuracy of the PINNs solutions (Basri et al., 2019; Cao et al., 2019). A series of methodologies, such as singular value decomposition (Gao et al., 2022), convolutional autoencoders (Kim et al., 2022), and Fourier transformation (Wang et al., 2021) have been suggested for tackling the dimensionality issues by transforming the network operations to lower frequency spaces. However, this issue is still an open question that needs to be addressed (Wang et al., 2022). We propose that a proper mathematical formulation of the system will have impact on the non-linearity and, thus, the ability of a PINN to represent the solution accurately. It is noted that defining features based on physics is a meaningful and established way of constraining machine learning models (Chao et al., 2022; Magzymov et al., 2022). However, the role of modifying the independent variables while representing the same PDE problem has not been explored and not in a PINN context.

This work investigates whether a PINN-based approach can effectively solve the 1D COUCSI problem, for the first time at both ET and LT periods. We also investigated how reformulating the COUCSI PDEs based on different independent variables (derived based on the physical characteristics of the system) may impact the PINN accuracy, the required network size, and the number of collocation points. To do that, by applying the Change-of-Variables technique, three different implementations of the normalized COUCSI flow equation are studied, considering (1) scaled position and time variables, (2) a self-similar form depending on only one variable, valid only before interaction with the closed boundary,

and (3) a form using the self-similar variable and square root of time as a second variable, valid for all times. The aim was the prediction of saturation profiles and recovery resulting from the 1D COUCSI system. We only used the same input as an FD numerical simulator; hence, no labeled training data from other sources (such as experiments, analytical or numerical solutions) are used to guide the PINNs training. The main questions of interest are:

- Can the PINN solver produce correct saturation and recovery profiles in the COUCSI system only by minimizing loss terms related to the PDE and corresponding initial/boundary conditions? How does the run-time of the PINN solution compare to that of traditional numerical simulations?
- Is there any advantage of reformulating the problem by Change-of-Variables in line with the physical behavior of the system? How is this reflected in how challenging it is to train the PINN and how well they predict? Can simpler networks and fewer collocation points be applied? How may it impact the run-time of solving the problem?
- To which level do the PINN solutions from different formulations preserve physical properties of the COUCSI system, such as self-similarity, Total Variation (TV) preservation, and the square root of time recovery behavior?

In the following section, we present the mathematical theory behind COUCSI and its formulations, the PINN methodology, and its implementation in this work. The results of applying PINN to solve the COUCSI problem for the different formulations for different test cases and different systematic training strategies are then presented. The work is then finalized with conclusions.

Mathematics of Spontaneous Imbibition

We investigate a two-phase flow system with immiscible and incompressible fluids. The porous medium is incompressible and homogeneous. The flow occurs in the horizontal direction without gravitational forces. All the faces are closed except the face at $x = 0$, where it is exposed to the wetting phase. The saturation of the wetting phase at the open face is fixed to s_w^{eq} , defined by a zero capillary pressure $P_c(s_w^{eq}) = 0$. The system is initially saturated with the non-wetting phase. The stated conditions result in 1D COUCSI, as shown in Figure 1. Darcy's law in 1D gives Darcy velocity (u_i) by writing:

$$u_i = -\lambda_i[\partial_x p_i], \quad \lambda_i = \frac{K k_{ri}}{\mu_i}, \quad (i = w, nw), \quad 1$$

where λ_i is mobility, p_i is pressure, K and k_{ri} are absolute permeability and relative permeability, respectively, and μ_i is viscosity. The index i refers to phase-specific properties for the wetting and non-wetting phases (w, nw). The conservation law determines the volumetric transport of phases in time:

$$\phi \partial_t (s_i) = -\partial_x (u_i), \quad (i = w, nw), \quad 2$$

where s_i is phase saturation. The saturations are constrained by volume conservation ($s_w + s_{nw} = 1$), and the positive capillary pressure function constrains the pressures ($p_{nw} - p_w = P_c(s_w)$). Combining these assumptions, we obtain the capillary diffusion equation describing 1D countercurrent spontaneous imbibition in the form of a second-order, elliptic PDE:

$$\phi \partial_t (s_w) = -K \partial_x (\lambda_{nw} f_w \partial_x P_c), \quad (0 < x < L) \quad 3$$

This implementation reduces the problem's dimensionality compared to Eq. 1 by removing the phase pressures and constraining the equations to a single PDE. The boundary and initial conditions are given by:

$$s_w(x = 0, t) = s_w^{eq}, \quad \partial_x s_w|_{x=L} = 0, \quad s_w(x, t = 0) = s_{wr} \quad 4$$

representing a fixed saturation at the inlet corresponding to zero capillary pressure, a closed boundary at $x = L$, and a uniform initial saturation (residual water saturation). When $s_w^{eq} = 1 - s_{or}$ (oil is immobile) the system is strongly water-wetting, while if $s_{wr} < s_w^{eq} < 1 - s_{nwr}$, the system is considered mixed-wet.

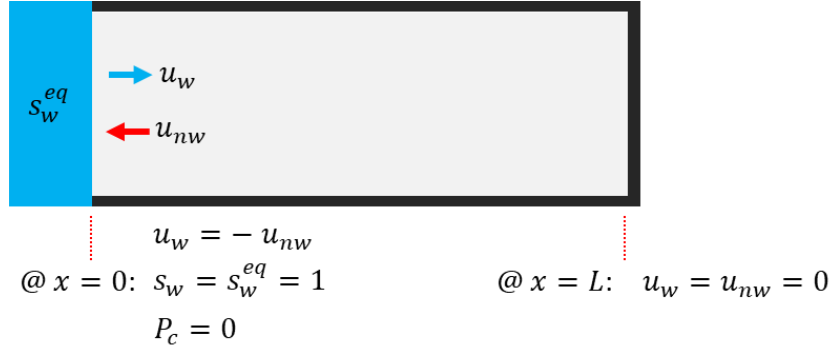


Figure 1: The COUCSI geometry and the applied boundary conditions. The core is initially saturated by the non-wetting phase and exposed to the wetting phase at $x = 0$. Other faces are closed to flow.

Scaled Representations

Three different scaled representations will be considered of the flow equations (Eqs. 2 or 3). The Change-of-Variables technique was used, which is defined as the substitution of the variables of a PDE by new variables that are a function of the original variables (Folland, 1999). Each representation has different properties and hence potential advantages related to producing accurate solutions with PINN, which will be investigated.

Normalized Diffusion Equation (XT formulation)

By defining normalized spatial and temporal variables X , and T , and saturation S_n the system of Eq. 3 and 4 can be written (see Appendix A for details) into an equivalent dimensionless form (Andersen, 2023b):

$$\partial_T S_n = \partial_X (\Lambda_n(S_n) \partial_X S_n), \quad (0 < X < 1) \quad 5$$

$$S_n(X = 0, T) = 1, \quad \partial_X S_n|_{X=1} = 0, \quad S_n(X, T = 0) = 0 \quad 6$$

The interval $0 < S_n < 1$ is where imbibition occurs. Λ_n is a scaled diffusion coefficient with a mean one over the imbibing saturations. This scaled representation captures all wetting states and input parameter combinations and only depends on the shape of $\Lambda_n(S_n)$. Eq 5 and 6 are called the XT-formulation. This formulation is valid in full-time (FT) period, i.e., both ET and LT.

Square Root of Time Full-time Solution (XY-formulation)

By replacing the temporal variable from T to $Y = T^{0.5}$ and use it together with X , i.e., $S_n = S_n(X, Y)$, we can develop a system that is valid for both ET and LT flow periods. When reformulating Eq. 5, we use Y in the spatial derivatives (Andersen, 2023a):

$$\partial_Y S_n = 2Y \partial_X (\Lambda_n(S_n) \partial_X S_n), \quad 7$$

$$S_n(X, Y = 0) = 0, \quad S_n(X = 0, Y) = 1, \quad \partial_X S_n|_{X=1} = 0 \quad 8$$

We refer to this system as the XY formulation.

Self-similar Early-time Solution (Z-formulation)

If we consider the time before the no-flow boundary is encountered, the 1D COUCSI system behaves in a self-similar way. The role of position and time can be combined into one variable $Z = X/T^{0.5}$ which determines the solution for a given function Λ_n , i.e., $S_n = S_n(Z)$. Using this variable, the system of Eq. 5 and 6 can be expressed as (Andersen, 2023a):

$$Z\partial_Z S_n = -2\partial_Z(\Lambda_n(S_n)\partial_Z S_n), \quad (0 < Z < \infty) \quad 9$$

$$S_n(Z = \infty) = 0, \quad S_n(Z = 0) = 1 \quad 10$$

with the exception that the closed boundary condition in Eq. 6 is replaced by obtaining the initial condition at an infinite distance. We call Eqs. 9 and 10 the Z-formulation.

Total Variation

The Total Variation (TV) concept in mathematics is the magnitude of the arclength of a curve related to a continuous function in an interval of interest (Harten, 1983). It can represent the amount of oscillation in a numerical solution and whether it increases with time; hence it is a valuable concept in numerical stability analysis (LeVeque, 2002). In this context, we consider the Total Variation in saturation along the core as a function of time:

$$TV(S_n(\cdot, t)) = \int_{x=0}^1 |\partial_x S_n| dx = \int_{x=0}^1 |dS_n| \quad 11$$

In other words, TV measures the total change in saturation along the core. As we have scaled the system to have a saturation equal to one at the inlet and to be zero initially, the TV is expected to be one at the ET. However, at LT, the saturation increases from zero at the closed boundary and hence reduces the TV. We thus expect our PINN solution to produce $TV = 1$ at the early time and TV declining from one towards zero (when the saturations are uniformly equal to 1) at the late time.

Physics-Informed Neural Networks

Physics-informed Neural Networks (PINNs) are a subset of scientific deep learning that try to solve PDEs/ODEs using a data-driven approach (Raissi et al., 2019). If $S_n(X, T)$ represents the solution of a 1D COUCSI system based on XT formulation, the PINNs model is defined as:

$$S_n(X, T) + \mathcal{N}[S_n; \lambda] = 0; \quad x \in \mathbb{R}, t \in \mathbb{R} \quad 12$$

Where $\mathcal{N}[S_n; \lambda]$ is the equivalent differential operator describing the investigating problem, and λ is its constitutive parameters. The PINNs model is developed by constraining $\mathcal{N}[S_n; \lambda]$ during the training, using the PDE representing the physical system and the constraining initial or boundary conditions. The training is carried out by utilizing automatic differentiation (AD) while back-propagation. By applying the successive chain rule, automatic differentiation computes gradients with an efficient computational cost.

The physical specification of the system is imposed on the PINN by the definition of a series of loss functions representing the mean squared errors (MSE) in the residuals of the system's underlying PDE (\mathcal{F}), initial conditions (\mathcal{J}), and boundary conditions (\mathcal{B}):

$$\mathcal{L}_{\mathcal{F}}(\theta) = \int_{\Omega} |\mathcal{F}(\mathcal{N})|^2 dx \quad 13$$

$$\mathcal{L}_J(\theta) = \int_{\Omega} |\mathcal{J}(\mathcal{N})|^2 dx \quad 14$$

$$\mathcal{L}_B(\theta) = \int_{\Omega} |\mathcal{B}(\mathcal{N})|^2 dx \quad 15$$

where \mathcal{L}_F denotes the loss due to deviation from the governing PDE in the domain Ω . Also, \mathcal{L}_J and \mathcal{L}_B are the losses related to the initial and boundary conditions, respectively. \mathcal{L}_B includes the conditions at both faces, i.e., $X = 0$, and $X = 1$ (except for Z formulation that is only valid at ET and only has a boundary condition at $X = 0$). If observation points (from sources like experiments or analytical/numerical solutions) are also available, an additional loss term representing the deviations from the true values may be defined. However, in this work, since no observation data is used in the training of the model, we neglected this loss term. Consequently, the total loss function is the weighted summation of all the defined losses:

$$\mathcal{L}_t(\theta, x) = \alpha_1 \mathcal{L}_F(\theta) + \alpha_2 \mathcal{L}_J(\theta) + \alpha_3 \mathcal{L}_B(\theta) \quad 16$$

Where α_i is the weight factor for each loss term. The above definition can also be defined for other forms of the COUCSI PDEs, i.e., XY and Z formulations. Based on the parameters of the applied formulation, we can define the PDE-, initial condition-, and boundary condition- residuals as below:

XT Formulation:

$$\mathcal{F}(X, T) = \partial_T S_n - \partial_X (\Lambda_n(S_n) \partial_X S_n) \quad 17$$

$$J = S_n(X, T = 0), \quad \mathcal{B}_1 = S_n(X = 0, T) - 1, \quad \mathcal{B}_2 = \partial_X S_n \quad 18$$

XY Formulation:

$$\mathcal{F}(X, Y) = \partial_Y S_n - 2Y \partial_X (\Lambda_n(S_n) \partial_X S_n) \quad 19$$

$$J = S_n(X, Y = 0), \quad \mathcal{B}_1 = S_n(X = 0, Y) - 1, \quad \mathcal{B}_2 = \partial_X S_n \quad 20$$

Z Formulation:

$$\mathcal{F}(Z) = \partial_Z S_n + \frac{2}{Z} \partial_Z (\Lambda_n(S_n) \partial_Z S_n) \quad 21$$

$$J = S_n(Z = \infty), \quad \mathcal{B}_1 = S_n(Z = 0) - 1, \quad \mathcal{B}_2 = \partial_Z S_n|_{(Y, Z = \frac{1}{Y})} \quad 22$$

\mathcal{B}_2 in Z formulation is theoretically trivial (in the ET period) and not obligatory in the training process; however, we calculated it at the deployment stage for quality check.

During our observations, we noticed that \mathcal{F} values near the flowing boundary were initially high, which had a significant impact on the PINN solutions. To address this, we omitted the \mathcal{F} values (in Eqs. 17 and 19) in the $X < 0.01$ range, during the training process.

Problem Setup

We considered two 1D COUCSI cases (A and B) with different frontal behavior. The rock/fluid properties were identical in both cases, except for their saturation functions. The capillary pressure curve for case A is generated based on Kumar et al. (2014). The saturation curves in case B are artificially generated to create a steeper saturation profile, different than case A. The main goal of having two cases is to investigate the capabilities of PINNs in capturing various flow behaviors. The basic rock and fluid properties are shown in Table 1. Also, the utilized relative permeability and capillary pressure curves are shown in Figure 2. Figure 2c shows the scaled capillary diffusion coefficient curves where the differences in the saturation functions could generate two different trends. We expect differences in the flow regimes

due to the differences in the scaled capillary diffusion curves. In this work, we utilized Corey-type relative permeabilities (Brooks & Corey, 1964),

$$k_{rw} = k_{rw}^* (S)^{n_w}, \quad k_{rnw} = k_{rnw}^* (1 - S)^{n_{nw}}, \quad 23$$

Here, n_w and n_{nw} are Corey exponents and k_{rw}^* and k_{rnw}^* are the relative permeability endpoints. Also, S is the normalized water saturation as:

$$S = \frac{S_w - S_{wr}}{1 - S_{or} - S_{wr}} \quad 24$$

The correlation introduced by Andersen et al. (2017) is used for the capillary pressure curves:

$$P_c = \frac{a_1}{(1 + k_1 S)^{n_1}} - \frac{a_2}{(1 + k_2 (1 - S))^{n_2}} + a_3 \quad 25$$

The parameters a_1 , a_2 , a_3 , k_1 , k_2 , n_1 , and n_2 determine the correlation shape. In case A, a_1 , a_2 , and a_3 are 15.52, 0.74, and 0.50 kPa, respectively, while in case B, a_1 , a_2 , and a_3 are 11.17, 5.17, and 5.00 kPa, respectively. Other parameters corresponding to the capillary pressure curves are similar and are presented in Table 1. The reference solutions for comparison with the PINN solutions were generated using a previously developed and verified core scale simulator IORCoreSim (Lohne et al., 2017) for numerical simulation of two-phase flow in porous media. The core was split equally into 400 grid cells, while the final scaled simulated time (35 hrs for case A and 10 hrs for case B) was divided into 120 report steps: the first 60 were equally spaced in square root time by $dt^{0.5} = 0.0167 \text{ hr}^{0.5}$ and the next 60 by $0.0819 \text{ hr}^{0.5}$ for case A, and similarly $dt^{0.5} = 0.0167 \text{ hr}^{0.5}$ and $0.0360 \text{ hr}^{0.5}$ for case B.

Table 1: Rock and fluid properties of the studied cases.

Parameters	Values	Parameters	Values	Parameters	Value
K	243.2 md	k_{rw}^*, k_{rnw}^*	1.0, 1.0	k_1	7
ϕ	0.2	n_w, n_{nw}	1.8, 1.4	k_2	0.4
L	0.06 cm	S_{wr}	0.0	n_1	2
μ_w, μ_{nw}	1.0, 1.0 cP	S_{or}	0.0	n_2	10

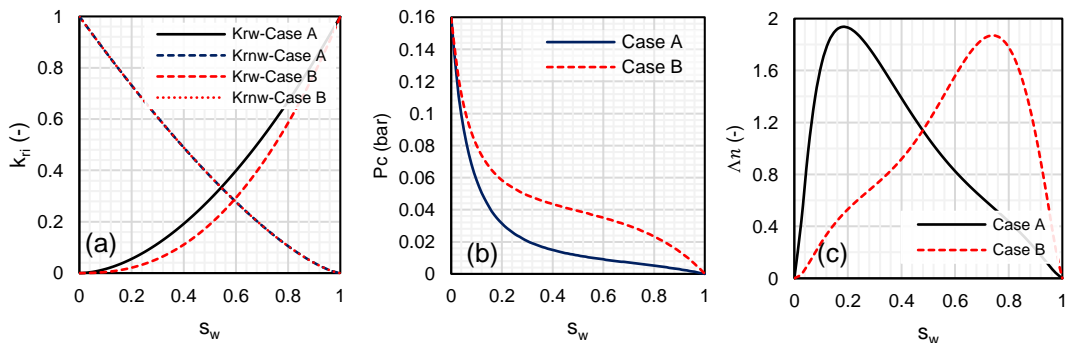


Figure 2: The applied saturation functions for two generated cases (A and B). (a) relative permeability, (b) capillary pressure, (c) scaled capillary diffusion coefficient Λ_n . The capillary pressure curve of case A is from Kumar et al. (2014). Case B was artificially generated for comparison.

Network and Training Setup

For each of the introduced formulations (i.e., XT , XY , Z), we used a fully connected feed-forward multilayer perceptron (MLP) network, called the latent network, sandwiched between an encoder and a decoder. The network should output S_n based on the corresponding inputs of each formulation, i.e., $S_n(X, T)$, $S_n(X, Y)$ or $S_n(Z)$. A schematic of the network setup is provided in Figure 3. The encoder is

composed of an MLP with two linear layers followed by a normalization layer (Ba et al., 2016), and the decoder consists of an MLP with three linear layers. In both the encoder and decoder, the layer widths were the same as the width of the latent network, which was 50 nodes. The role of the encoder is to transform the dimension of the PINN's input to the width of the latent network by matrix multiplication, and the decoder maps the latent network output to the expected PINN output dimension. The latent network is composed of an MLP with five hidden layers with the \tanh activation function and a width of 50 nodes. Fourier and inverse Fourier transform operations are performed on the input and output of the latent network, as discussed by Li et al. (2020). Performing the calculations in Fourier space improved the PINN performance and was applied as it is known to resolve deficiencies of standard PINNs in capturing high-frequency elements of the problem (Rahaman et al., 2018). In the output of the PINN, we set a rectifier function to make sure $0 \leq S_n \leq 1$.

Based on the mathematical definition of the investigated formulation, the model may have one input (for the Z formulation) or two inputs (for XT , and XY formulations). However, all the formulations used the same network architecture/size to simplify comparisons. A relatively large model was chosen to provide enough network complexity to capture the solution for all formulations. A sensitivity analysis of network size is carried out later to examine the possibility of simpler networks.

The number of collocation points in the spatial dimension (n_x or n_z) were chosen based on one hundred equally spaced points. In the temporal dimension, the number of collocation points (n_T) was 45 for both cases, in the FT simulations; approximately 1/3 of the points were in the ET region, and the remaining were in the LT region. The temporal points were increasing by constant DY values, up to the total time. The model was trained by consolidating all collocation points into a singular batch (fully batched), resulting in a single backpropagation calculation per epoch.

The trainable parameters in the network were initialized using a uniform random scheme. The gradient-based Adam optimizer (Kingma & Ba, 2014) was used for training the network with the starting learning rate $1e-4$ and weight-decay $1e-5$. We gradually reduced the learning rate by one order of magnitude during the training. The training was continued until the reduction in the loss term stopped. In all cases, the training could be terminated after $n_{ep}=4000$ epochs.

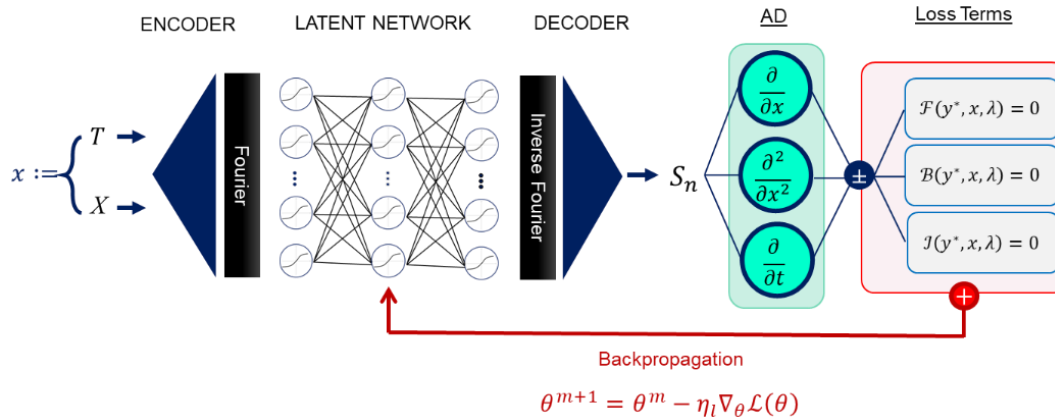


Figure 3: The architecture of the PINN based on the $S_n(X, T)$ formulation. Based on the applied PDE form, the input can also be X and Y for the XY PDE, and only Z for the Z PDE. The neurons in the latent network were activated by the \tanh activation function.

Results

Early- and full-time solutions

Results of the trained PINN solutions are presented in this section for cases A and B, using the three formulations introduced previously. The mean absolute error (MAE) values for PINN solutions (Saturation and Recovery factor) are shown in Figure 4. The values are separated based on ET, LT, or FT periods. The complete MAE values for the loss terms and solution outputs (saturation, capillary pressure,

and recovery factor) are summarized in Appendix B, Table A1. The MAEs are calculated by evaluating and comparing the FD and PINN solutions at the same collocation points. P_c is calculated from S_n using the capillary pressure correlation (Eq. 25), and recovery factor (RF) is defined as the average water saturation in the core at each time. The reported values from PINN correspond to the training after 4000 epochs. For each case and formulation, the FD and PINN saturation solutions, the absolute errors between them, and PDE residuals are illustrated in Figure 5 in 2D plots vs. spatial locations and time (Y).

All three formulations could capture the solutions of both COUCSI cases with reasonable accuracy. Figure 4 shows that the XY formulation performed superior in the FT period with the saturation MAE equal to 0.009 for both cases A and B, with roughly 50% less error compared to the XT formulation with MAE equal to 0.019 (case A) and 0.021 (case B). During the ET period, the Z formulation, with the S_n , the mean MAE of ~ 0.012 was superior to both other formulations (mean MAE ~ 0.030 for XT and ~ 0.014 for XY) in both cases. The same trends in performance were seen in Table A1 regarding the MAE of capillary pressure and recovery factor. Overall, there was a more significant error in ET as compared to LT, which can be attributed to PINN's inability to effectively minimize the loss term in points located near the flowing boundary.

One crucial factor that influenced the efficacy of PINN was the approach used for sampling collocation points. The comprehensive analysis is presented in Appendix D. Our findings indicate that selecting points based on constant DY intervals led to a notable decrease in the required data points. Furthermore, when the same number of data points were used, the model based on constant DY intervals exhibited superior performance. It is worth noting that the COUCSI problem exhibits a more uniform flow rate on the Y coordinate, than the T coordinate. Another crucial point to consider is that the XY and Z formulations performed better with lower numbers of collocation points (See Figure A2), which is highly beneficial for the rapid solution of the COUCSI problem in practical scenarios.

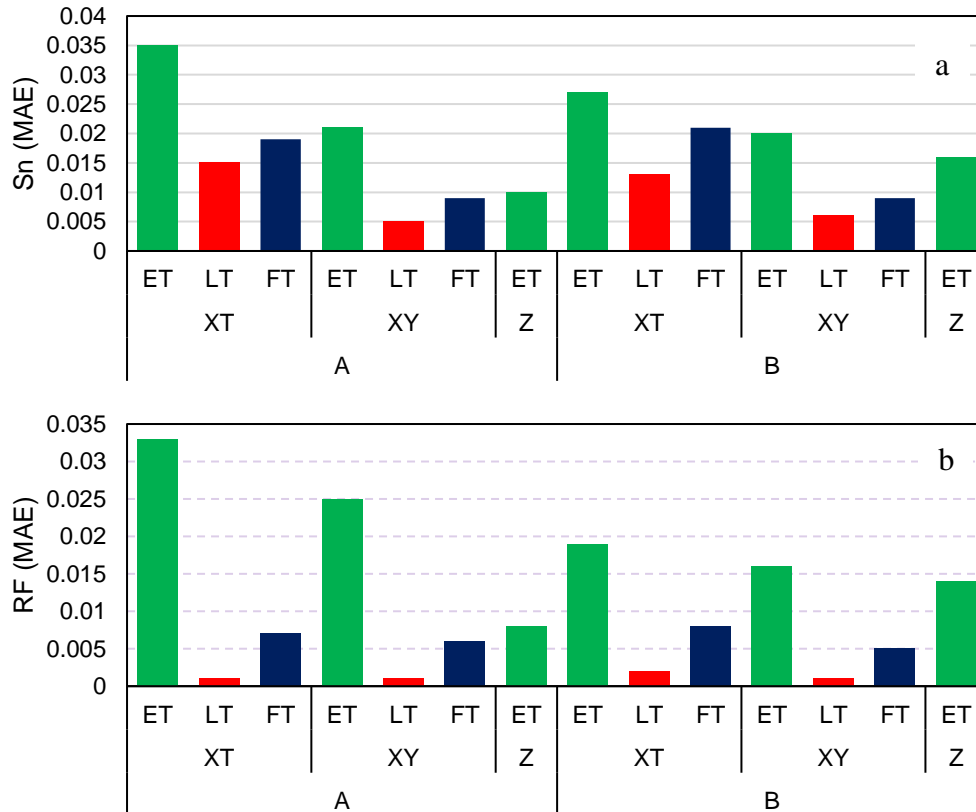


Figure 4: The final error (MAE) of PINN predictions for all three formulations, separated by early-time (ET), late-time (LT), and full-time (FT) periods. a) S_n , b) RF.

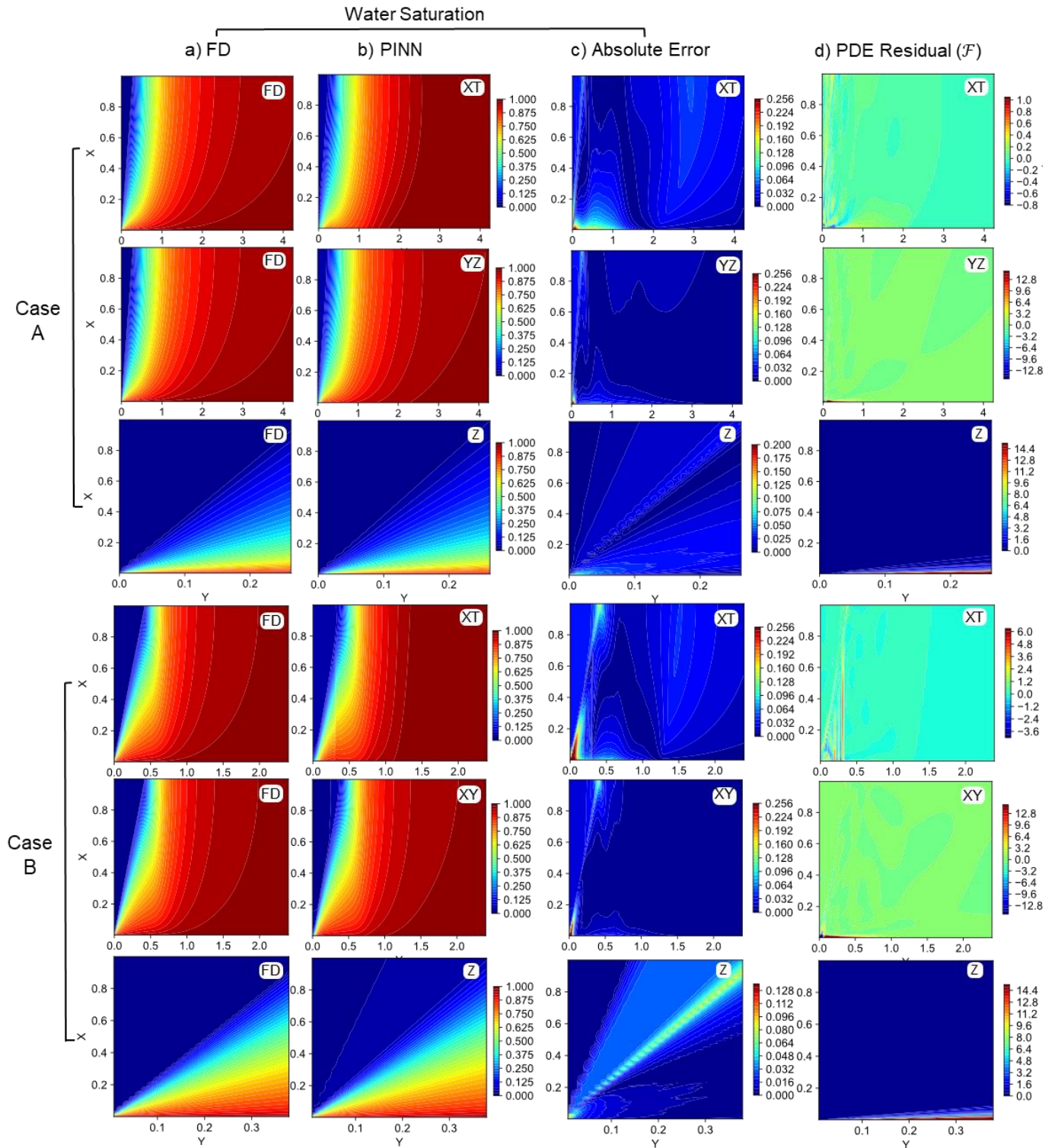


Figure 5: The contour maps of FD versus PINNs solutions (S_n) for different formulations. The solutions for Z-formulation only show the ET period; a) baseline FD, b) PINNs, c) absolute error, d) PDE residuals (in each formulation, the scales are different, so the numbers are not directly comparable).

Figure 6 shows how the total loss term (\mathcal{L}_t) and saturation MAE of the networks evolve with training. Note that the predicted saturations are obtained from training the networks to satisfy the loss terms of the PDEs, initial conditions, and boundary conditions, but not data directly. The error is based on comparing predicted saturations with the FD saturation values. After 500-1000 epochs, the PINN solution errors stabilized very close to the FD values, even with low learning rates; after that, we continued the training for fine-tuning the solutions. The solutions could have been achieved faster by choosing a higher starting learning rate.

Nonetheless, when evaluating the effectiveness of PINN across various formulations, it was found that the XY and Z formulations achieved convergence towards the correct solutions in fewer epochs than the XT formulation. The comparison of run-time for PINN in Appendix F also indicates that the XY and Z formulations provided quicker solutions as compared to the XT formulation. (See Figure A5). Moreover, all the models demonstrated a satisfactory correlation between the total loss term value and the saturation profile's MAE (as depicted in Figure A1), signifying the dependability of the PINN solution in the absence of any knowledge pertaining to the true solutions.

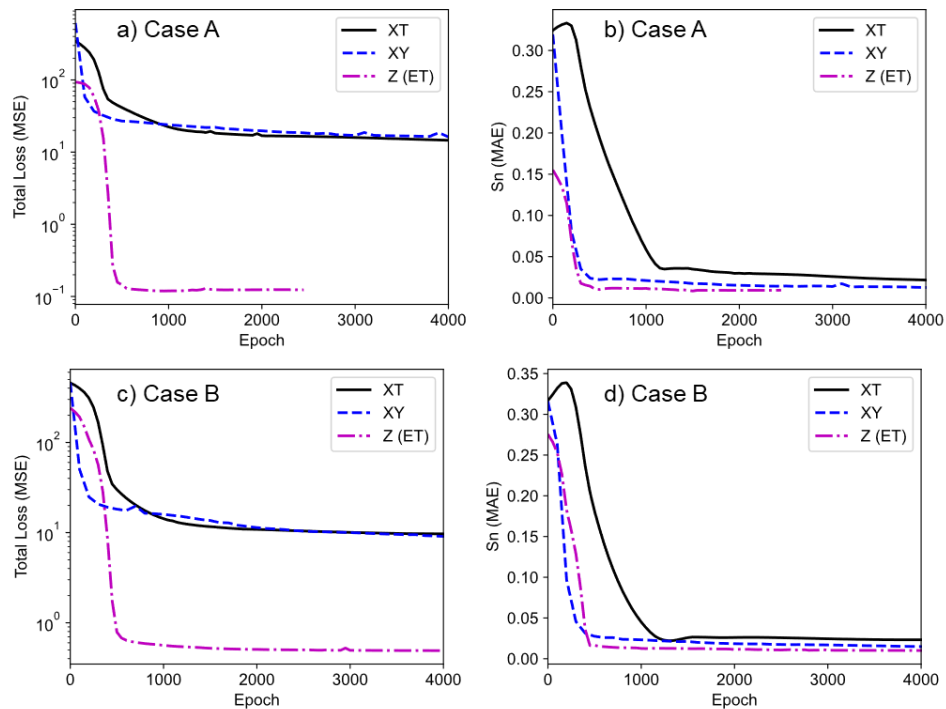


Figure 6: The trend of the total loss term, and Sn MAE versus epochs during the training for different PDE formulations. a-b) Case A, c-d) Case B.

Figure 7 compares the saturation and recovery profiles for XT and XY formulations at all times. Both formulations could capture the recovery profile acceptably. In both cases, the XY formulation could predict the profiles better in the starting and finishing periods of imbibition ($T < 0.01$ and $T > 1$), while the XT formulation performed better in the intermediate periods. The overall error in the XY formulation was lower than the XT formulation, as shown in **Error! Reference source not found.**

Comparing the ET saturation profiles of different formulations (XT and XY in Figure 9, and Z formulation in Figure 8) shows that all PDE PINN formulations capture the overall trend in the ET period. The most challenging aspect seems to be capturing the boundary conditions where it is seen that the saturations at

$X = 0$ approach values less than one, and the saturations at the imbibition front tend to overshoot the FD solution. This difficulty causes a greater MAE in saturations at ET compared to LT, as previously depicted in Figure 4. The solutions overlap better at central saturations and for saturation profiles that have advanced further into the core. The mentioned challenges at the boundaries were handled better by the Z formulation than XT and XY formulations.

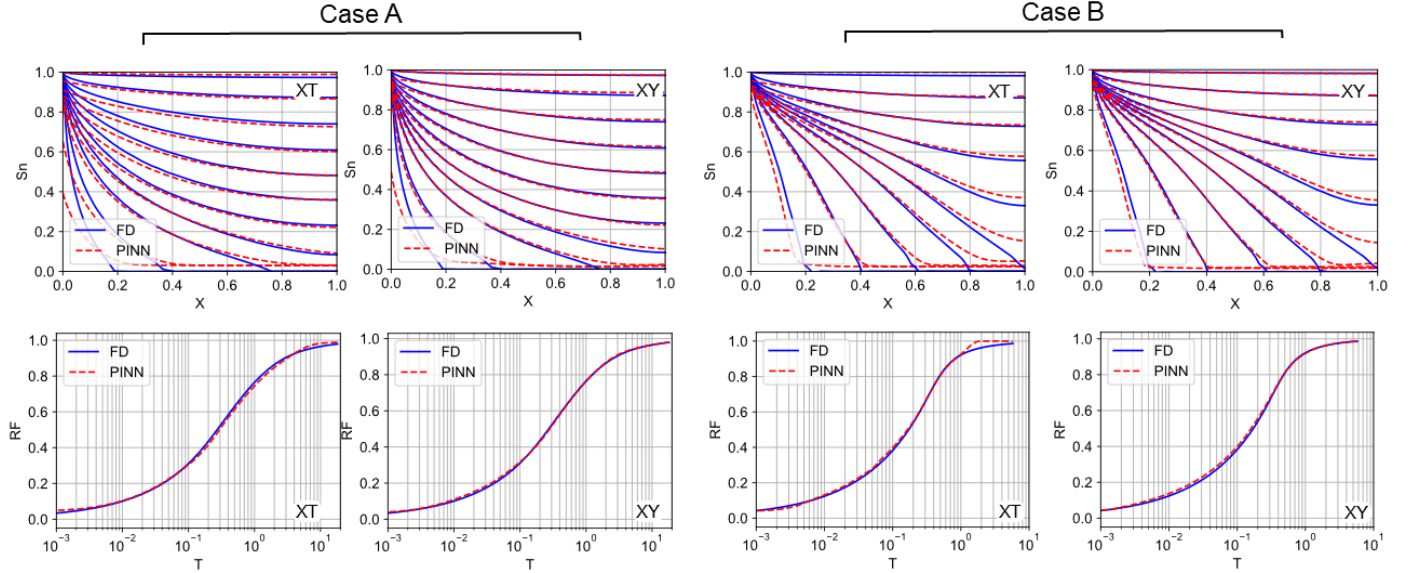


Figure 7: The production profile for the XT and XY formulations in the entire COUCSI period. a) Saturation Profile, b) Recovery profile.

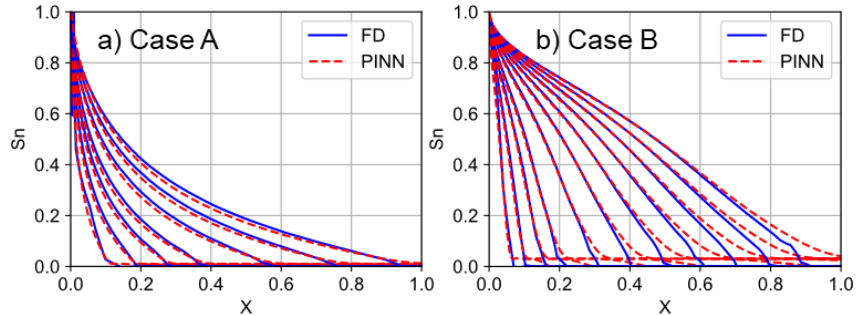


Figure 8: Saturation profiles $S_n(X)$ obtained from Z formulation for the ET period of COUCSI. a) Case A, b) Case B.

In Figure 9, spatial saturation profiles (S_n vs. Z) and recovery profiles (RF vs. Z) are shown in the ET period. Figure 9a shows the saturation profiles plotted versus the similarity variable Z for the different timesteps. Ideally, we expect all the profiles to overlap because of the self-similarity of COUCSI at ET. In the Z formulation, all the profiles are matched. By design, it preserves self-similarity as the PINN solution is only a function of Z (different ranges of Z follow from considering different times). The XT and XY formulations failed in giving proper self-similar solutions at the beginning times of flow: the saturations of a given Z -value on some curves was lower than the correct values.

Figure 9b checks if recovery predicted from the PINN solutions followed proportionality with the square root of time. Semi-analytical solutions for 1D COUCSI by McWhorter & Sunada (1990) have proven that recovery at ET follows a linear trend versus the square root of time (linearity with Y). The Z

formulation produced a straight line for recovery against Y during ET, where the slope matched well, but not precisely, with the FD solution. The XY formulation followed the FD line well but was not a perfectly straight line; the slope rather slightly increased with Y . This was the same for the XT formulation, where the PINN solution more notably failed to give zero recovery at zero time but corresponded well with the FD solution at higher values of Y .

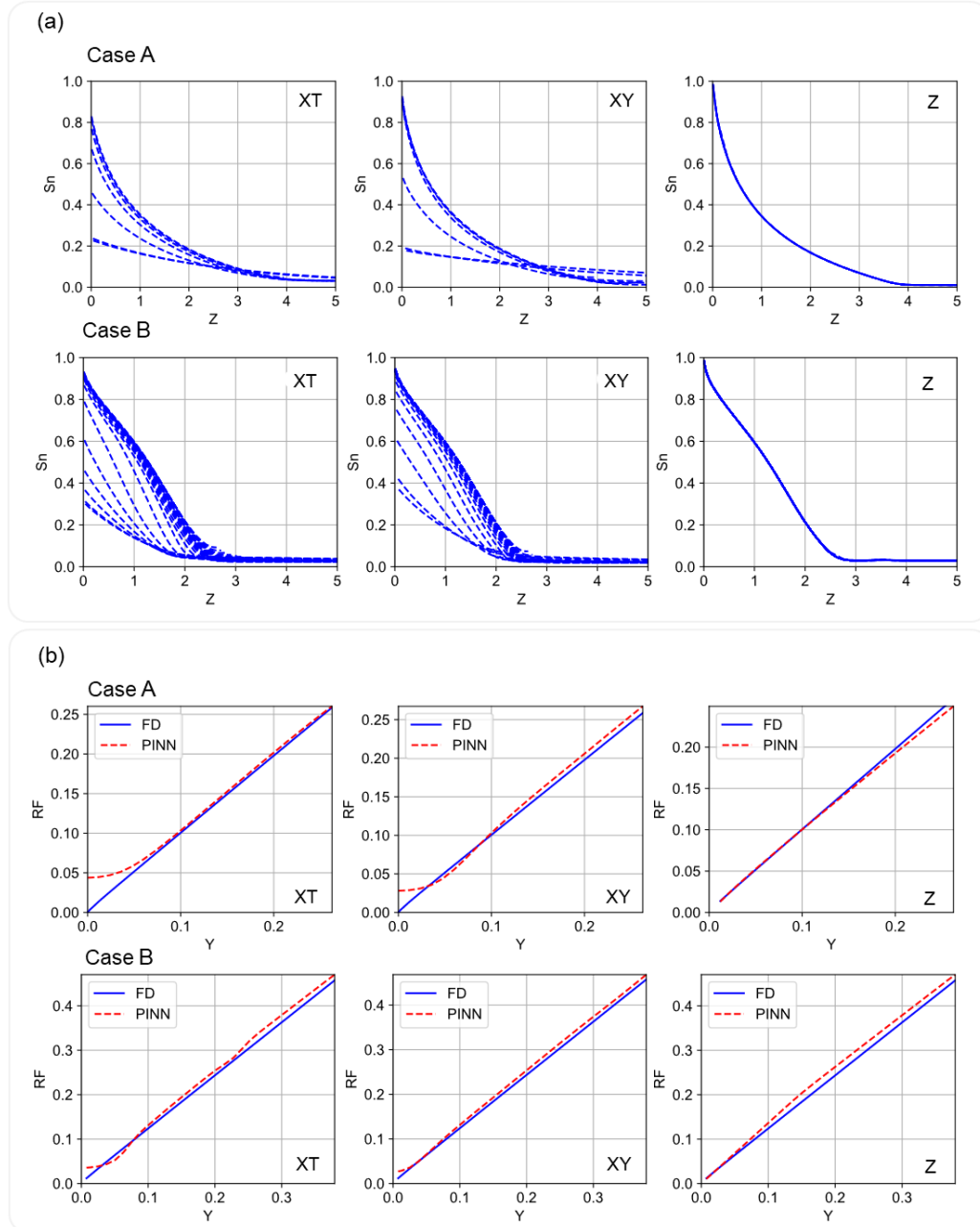


Figure 9: The performance of PINNs with different PDE formulations (XT, XY, Z) for the ET period of COUCSI. a) Saturation profiles vs. similarity variable (Z), b) Recovery factor versus square root of time (Y) for FD and PINN solutions.

The TV behavior of different solutions in the ET period are compared in Figure 10 as a function of scaled time T . The curves show that the XT formulation performed weakly in preserving the TV property of the model through time and that the value stayed far below 1. XY formulation could preserve the TV at a higher value, while the Z formulation managed to stay fairly constant close to one. In the XT solution, TV

increased with T , indicating the inlet saturation increased with time. As this saturation was more fixed in the other formulations, TV did not change with time in the beginning for those cases. The TV decreased towards the end in all formulations because saturations were predicted to reach the closed boundary too early. This was a bigger problem in Case A than B and more severe for the XT and XY formulations than the Z formulation. A majority of the deviations of TV from 1 originate from the weaknesses of the PINN in sufficient handling of the J and \mathcal{B}_1 terms (see **Error! Reference source not found.**).

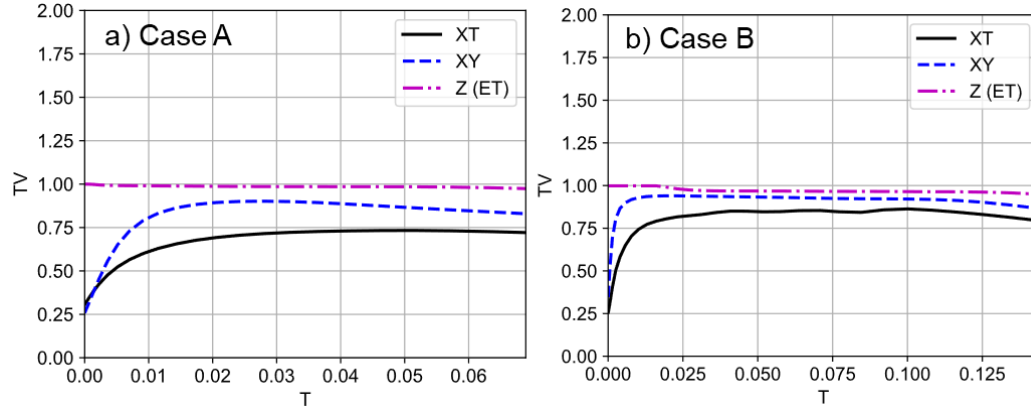


Figure 10: The calculated total variation (TV) from the PINN solutions with different PDE formulations (XT , XY , Z) for the ET period of COUCSI. a) Case A, b) Case B.

To have a better overview of the impact of changing formulations in PINNs, we also compared the loss landscape for all three formulations in Figure 11 (details are provided in Appendix C). It should be noted that the center of each landscape is related to the trained PINN model. Figure 11a shows a chaotic, non-convex landscape with an approximately ambiguous global minima, while XY formulation clearly shows a smooth surface with a trivial global minima. Z formulation also showed a smooth loss landscape with a clear global minima. The comparison of the loss landscapes reveals that changing the variables of the PDE from XT to XY and Z formulations could significantly enhance the convexity and smoothness of the loss landscape and provide training trajectories that are more explicit and dependable. This enhancement results in a reduction in the number of required collocation points (refer to Appendix D), the necessary network size (refer to Appendix E), as well as the run-time of the model (refer to Appendix F).

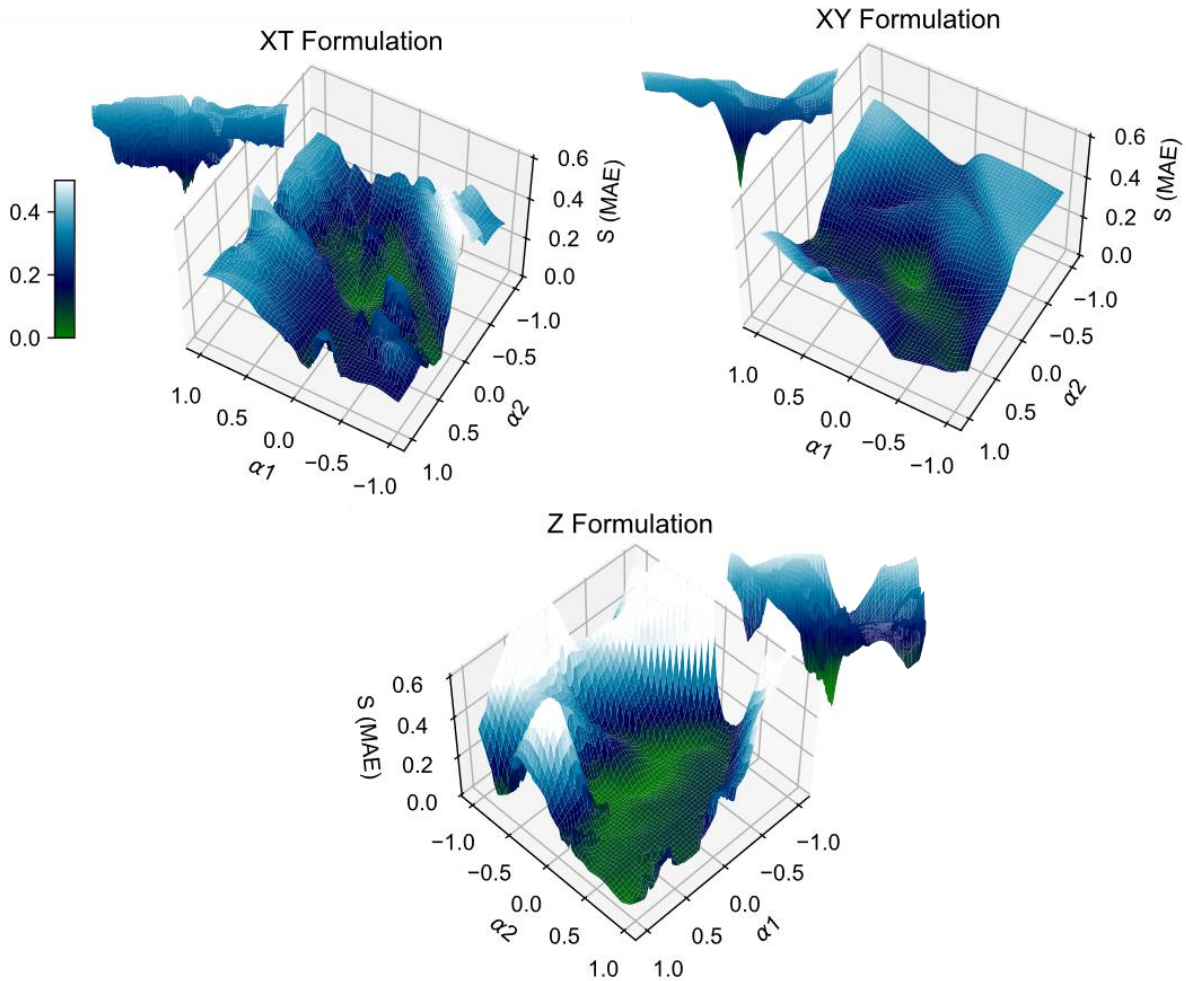


Figure 11: 3D loss landscape, generated by linear mixing of two different initial directions with the trained model parameters. A logarithmic side-view representation of the loss-landscapes are also shown for more clarity. a) XT, b) XY, c) Z

Discussion

This study focused on PINN-based solving of the two-phase 1D COUCSI phenomena with different equivalent PDE formulations obtained from Change-of-Variables technique. PINN could successfully solve all the PDE formulations with acceptable errors. Changing the PDE variables in accordance with the physical properties of the system, such as the square root of time flow, showed to have the potential to enhance the performance of PINN in various ways, including accuracy of solutions and computational efficiency of the models.

A severe problem in many of the PINN models during the training was that the optimizer could quickly lose track of the actual solution and converge to the trivial solution with $S_n x, t = 1$ in all spatial and temporal values. We found that the problem can be tackled by choosing approximately equal weight factors for different terms in the loss function and choosing enough resolution of the collocation points, especially in points close to the initial/boundary regions. A practical problem with the Z formulation was that at $T = 0$, $Z_{max} = \frac{1}{\gamma} \rightarrow \infty$ and the interval with non-trivial solutions becomes very small compared to

the full interval. We tackled this problem by adding a small constant to the denominator when selecting collocation points.

The total variation TV is a useful property to evaluate mathematical systems and their numerical schemes. In this work, we utilized this concept to track the PINN results' validity for the different cases. In the problems studied in this work, the TV should stay constant, equal to one, at ET and then decline towards zero. The preservation was satisfied to a reasonable level in Z formulation. For the XT (and to a less extent, XY) formulation, TV varied more dynamically, starting and ending at lower values than the others, while for all the formulations, TV declined towards the end. The difference from one was related to lower saturation at the inlet than the mathematical boundary condition. It stayed constant for Z formulation, while for XT (and XY), it changed dynamically. The late decline was related to PINN saturations reaching the no-flow boundary too soon. We believe the TV property can be better maintained by inclusion as an additional loss term in the training process or by better capturing the boundary condition loss terms. There are generally two different approaches for defining this term: 1) the TV may be calculated analytically using automatic differentiation; this approach should be more accurate; however, it may add significant computational load to the optimizer. 2) the more efficient approach is the definition of the problem in a discretized approach where it still has acceptable accuracy but takes much lower computational costs.

In addition to capturing the PDE, IC, and BC terms, we note that the PINN should capture two important transitions: the finite saturation gradient at the front jumps to zero ahead of the front. As seen in Figures 4 and 6, the PINN's main challenge was capturing the abrupt change in gradient at the front and the self-similarity of the ET solution when two variables were involved in the system formulation. In case B, the gradient was steeper at the front, and hence the change to zero gradients ahead of the front was more abrupt, which is believed to explain the incredible difficulty of training the solutions to this case.

We could show the feasibility of applying a pure PINN-based approach for solving benchmark core-scale phenomena with different formulations. The merit of using different formulations was that we could show the potentials of using the Change-of-Variables technique for improving the performance of PINNs in terms of collocation point selection, network complexity and by reducing the complexity of PDEs and simplify complicated differentiations. We believe the approach can be extended to other engineering processes. However, we see a potential to achieve lower error values and reduce the computational load during training. Given its relatively short run-time compared to numerical simulations, PINN-based solutions are a promising approach for obtaining quick approximations of forward problems. However, PINNs may be even more advantageous for inverse problems, where the iterative nature of numerical simulation methods can significantly increase computational time. Our future work will explore the use of PINNs for inverse solutions in porous media flow processes.

Conclusions

In this work, we studied the performance of PINNs in solving the two-phase 1D COUCSI problem. Using Change-of-Variables, the system was expressed in three equivalent PDE formulations (XT, XY, and Z), and we compared the resulting performance of the PINNs during early- or late-time for two simulation cases A and B. The following conclusions were obtained:

- The PINN solver could acceptably solve the 1D COUCSI problem, as shown for two different cases in early and late time flow regimes, with the MAE of saturations around 0.01 for the ET and 0.03 for the full imbibition time. The error was typically least for Z formulation (only ET), followed by XY, then XT. The errors were typically located at the inlet, at the imbibition front and at the closed boundary when the front arrived there.
- Total Variation of saturation was used to evaluate the saturation profile solutions with time. A difference from 1 at ET indicates that the solution does not meet the boundary and initial conditions properly (or has oscillations, which was not encountered).

- The Change-of-Variables technique helped in transforming the coordinates of the imbibition problem into a neater space which had lower prediction errors and was closer to the physical properties of the COUCSI problem, such as self-similar saturation profiles, TV preservation and the square root of time recovery behavior in the ET region. Especially, the Z formulation, by definition, obtained self-similar profiles, square root of time recovery, and constant TV. In contrast, XT and XY formulations obtained profiles that did not fully overlap at ET, recoveries that only approximately followed the square root of time and were not identical to zero at time zero, and TVs that varied with time. XY formulation, however, performed much better than XT from these perspectives. The TV values at ET were closer to 1 for Z, then XY, then XT formulations indicating a difference in how well the initial and boundary conditions were captured. The comparison of loss landscapes also revealed that the XY and Z formulations had a higher degree of convexity as compared to the XT formulation.
- By Change-of-Variables, fewer collocation points were required depending on which formulation and variable sampling procedure was used. Both for XT and XY systems, fewer temporal points are needed if they are selected based on constant DY (fixed square root of time difference) compared to constant DT (fixed time difference) and lower errors are obtained. The constant DY sampling focuses on both the early and late times. At a given number of temporal points, the XY formulation had less error than the XT formulation. Also, The Change-of-Variable technique could help reduce the network size.
- The run-time of PINN to achieve a saturation MAE of 0.03 was shorter than that of MRST, while it was longer if one aimed to attain lower MAE values. Overall, it can be inferred that the solutions provided by PINN are computationally efficient if one requires a fast estimation of the accurate solutions.

Acknowledgments

The authors acknowledge the Research Council of Norway and the industry partners of NCS2030 – RCN project number 331644 – for their support. Also, we appreciate Validé AS for partially granting this project under the Plogen program.

References

- Abbasi, J., & Andersen, P. Ø. (2022). Theoretical comparison of two setups for capillary pressure measurement by centrifuge. *Heliyon*, 8(9), e10656. <https://doi.org/10.1016/J.HELIYON.2022.E10656>
- Almajid, M. M., & Abu-Al-Saud, M. O. (2022). Prediction of porous media fluid flow using physics informed neural networks. *Journal of Petroleum Science and Engineering*, 208. <https://doi.org/10.1016/j.petrol.2021.109205>
- Andersen, P. Ø. (2021). A semi-analytical solution for shale gas production from compressible matrix including scaling of gas recovery. *Journal of Natural Gas Science and Engineering*, 95, 104227.
- Andersen, P. Ø. (2023a). Insights from Boltzmann transformation in solving 1D counter-current spontaneous imbibition at early and late time. *Advances in Geo-Energy Research*, 7(3), 164–175.
- Andersen, P. Ø. (2023b). Early- and late-time prediction of counter-current spontaneous imbibition, scaling analysis and estimation of the capillary diffusion coefficient. *Transport in Porous Media*.
- Andersen, P. Ø., Skjæveland, S. M., & Standnes, D. C. (2017). A novel bounded capillary pressure correlation with application to both mixed and strongly wetted porous media. *Abu Dhabi International Petroleum Exhibition & Conference*.
- Ba, J. L., Kiros, J. R., & Hinton, G. E. (2016). Layer normalization. *ArXiv Preprint ArXiv:1607.06450*.

- Barenblatt, G. I., Entov, V. M., & Ryzhik, V. M. (1990). *Theory of fluid flows through natural rocks* (Vol. 395). Springer.
- Basri, R., Jacobs, D., Kasten, Y., & Kritchman, S. (2019). The Convergence Rate of Neural Networks for Learned Functions of Different Frequencies. *Advances in Neural Information Processing Systems*, 32. <https://doi.org/10.48550/arxiv.1906.00425>
- Bjørnara, T. I., & Mathias, S. A. (2013). A pseudospectral approach to the McWhorter and Sunada equation for two-phase flow in porous media with capillary pressure. *Computational Geosciences*, 17(6), 889–897. <https://doi.org/10.1007/S10596-013-9360-4/METRICS>
- Bourbiaux, B. J., & Kalaydjian, F. J. (1990). Experimental study of cocurrent and countercurrent flows in natural porous media. *SPE Reservoir Engineering*, 5(03), 361–368.
- Brooks, R. H., & Corey, A. T. (1964). Hydraulic properties of porous media and their relation to drainage design. *Transactions of the ASAE*, 7(1), 26–28.
- Cao, Y., Fang, Z., Wu, Y., Zhou, D. X., & Gu, Q. (2019). Towards Understanding the Spectral Bias of Deep Learning. *IJCAI International Joint Conference on Artificial Intelligence*, 2205–2211. <https://doi.org/10.48550/arxiv.1912.01198>
- Chao, M. A., Kulkarni, C., Goebel, K., & Fink, O. (2022). Fusing physics-based and deep learning models for prognostics. *Reliability Engineering & System Safety*, 217, 107961.
- Cil, M., & Reis, J. C. (1996). A multi-dimensional, analytical model for counter-current water imbibition into gas-saturated matrix blocks. *Journal of Petroleum Science and Engineering*, 16(1–3), 61–69.
- Daw, A., Bu, J., Wang, S., Perdikaris, P., Karpatne, A., & Tech, V. (2022). *Mitigating Propagation Failures in PINNs using Evolutionary Sampling*. <https://doi.org/10.48550/arxiv.2207.02338>
- Deng, L., & Pan, Y. (2021). Application of physics-informed neural networks for self-similar and transient solutions of spontaneous imbibition. *Journal of Petroleum Science and Engineering*, 203. <https://doi.org/10.1016/J.PETROL.2021.108644>
- Fokas, A. S., & Yortsos, Y. C. (1982). On the exactly solvable equation $S_t = [(\beta S + \gamma)^2 - 2 S_x]_x + \alpha(\beta S + \gamma)^2 - 2 S_x$ Occurring in Two-Phase Flow in Porous Media. *SIAM Journal on Applied Mathematics*, 42(2), 318–332. <https://doi.org/10.1137/0142025>
- Folland, G. B. (1999). *Real analysis: modern techniques and their applications* (Vol. 40). John Wiley & Sons.
- Fraces, C. G., & Tchelepi, H. (2021). Physics Informed Deep Learning for Flow and Transport in Porous Media. *Society of Petroleum Engineers – SPE Reservoir Simulation Conference 2021, RSC 2021*. <https://doi.org/10.48550/arxiv.2104.02629>
- Gao, Y., Cheung, K. C., & Ng, M. K. (2022). *SVD-PINNs: Transfer Learning of Physics-Informed Neural Networks via Singular Value Decomposition*. <https://doi.org/10.1109/SSCI51031.2022.10022281>
- Harten, A. (1983). High resolution schemes for hyperbolic conservation laws. *Journal of Computational Physics*, 49(3), 357–393. [https://doi.org/10.1016/0021-9991\(83\)90136-5](https://doi.org/10.1016/0021-9991(83)90136-5)
- Karniadakis, G. E., Kevrekidis, I. G., Lu, L., Perdikaris, P., Wang, S., & Yang, L. (2021). Physics-informed machine learning. In *Nature Reviews Physics* (Vol. 3, Issue 6, pp. 422–440). Springer Nature. <https://doi.org/10.1038/s42254-021-00314-5>
- Kashchiev, D., & Firoozabadi, A. (2003). Analytical Solutions for 1D Countercurrent Imbibition in Water-Wet Media. *SPE Journal*, 8(04), 401–408. <https://doi.org/10.2118/87333-PA>
- Khan, A. S., Siddiqui, A. R., Abd, A. S., & Alyafei, N. (2018). Guidelines for Numerically Modeling Co- and Counter-current Spontaneous Imbibition. *Transport in Porous Media*, 124(3), 743–766. <https://doi.org/10.1007/S11242-018-1093-3/FIGURES/20>
- Kim, Y., Choi, Y., Widemann, D., & Zohdi, T. (2022). A fast and accurate physics-informed neural network reduced order model with shallow masked autoencoder. *Journal of Computational Physics*, 451, 110841.
- Kingma, D. P., & Ba, J. L. (2014). Adam: A Method for Stochastic Optimization. *3rd International Conference on Learning Representations, ICLR 2015 – Conference Track Proceedings*. <https://arxiv.org/abs/1412.6980v9>

- Krogstad, S., Lie, K., Møyner, O., Nilsen, H. M., Raynaud, X., & Skaflestad, B. (2015). MRST-AD – an Open-Source Framework for Rapid Prototyping and Evaluation of Reservoir Simulation Problems. In *SPE Reservoir Simulation Symposium*. Society of Petroleum Engineers. <https://doi.org/10.2118/173317-MS>
- Kumar, S., Awang, M., Abbhas, G., Farouque, K., Ahmed -Weatherford, S., Tool, O., East -Pakistan, M., & Teknologi Petronas -Malaysia, U. (2014). *OTC-24715-MS Simulation Protocol for Core Flooding: Relative Permeability and Capillary Pressure Analysis*. <http://onepetro.org/OTCASIA/proceedings-pdf/14OTCA/AII-14OTCA/OTC-24715-MS/1504151/otc-24715-ms.pdf/1>
- LeVeque, R. J. (2002). Finite Volume Methods for Hyperbolic Problems. *Finite Volume Methods for Hyperbolic Problems*. <https://doi.org/10.1017/CBO9780511791253>
- Li, H., Xu, Z., Taylor, G., Studer, C., & Goldstein, T. (2018). Visualizing the loss landscape of neural nets. *Advances in Neural Information Processing Systems*, 31.
- Li, Y., Morrow, N. R., & Ruth, D. (2003). Similarity solution for linear counter-current spontaneous imbibition. *Journal of Petroleum Science and Engineering*, 39(3–4), 309–326. [https://doi.org/10.1016/S0920-4105\(03\)00071-8](https://doi.org/10.1016/S0920-4105(03)00071-8)
- Li, Y., Ruth, D., Mason, G., & Morrow, N. R. (2006). Pressures acting in counter-current spontaneous imbibition. *Journal of Petroleum Science and Engineering*, 52(1–4), 87–99. <https://doi.org/10.1016/J.PETROL.2006.03.005>
- Li, Z., Kovachki, N., Azizzadenesheli, K., Liu, B., Bhattacharya, K., Stuart, A., & Anandkumar, A. (2020). *Fourier Neural Operator for Parametric Partial Differential Equations*. <https://doi.org/10.48550/arxiv.2010.08895>
- Lohne, A., Nødland, O., Stavland, A., & Hiorth, A. Aksel. (2017). A model for non-Newtonian flow in porous media at different flow regimes. *Comput Geosci*, 21, 1289–1312. <https://doi.org/10.1007/s10596-017-9692-6>
- Magzymov, D., Ratnakar, R. R., Dindoruk, B., & Johns, R. T. (2022). Evaluation of machine learning methodologies using simple physics based conceptual models for flow in porous media. *Journal of Petroleum Science and Engineering*, 219, 111056. <https://doi.org/10.1016/J.PETROL.2022.111056>
- March, R., Doster, F., & Geiger, S. (2016). Accurate early-time and late-time modeling of countercurrent spontaneous imbibition. *Water Resources Research*, 52(8), 6263–6276.
- Mason, G., & Morrow, N. R. (2013). Developments in spontaneous imbibition and possibilities for future work. *Journal of Petroleum Science and Engineering*, 110, 268–293. <https://doi.org/10.1016/j.petrol.2013.08.018>
- McWhorter, D. B., & Sunada, D. K. (1990). Exact integral solutions for two-phase flow. *Water Resources Research*, 26(3), 399–413. <https://doi.org/10.1029/WR026i003p00399>
- Nabian, M. A., Gladstone, R. J., & Meidani, H. (2021). Efficient training of physics-informed neural networks via importance sampling. *Computer-Aided Civil and Infrastructure Engineering*, 36(8), 962–977. <https://doi.org/10.1111/mice.12685>
- Rahaman, N., Arpit, D., Baratin, A., Draxler, F., Lin, M., Hamprecht, F. A., Bengio, Y., & Courville, A. (2018). On the spectral bias of deep neural networks. *ArXiv Preprint ArXiv:1806.08734*, 4.
- Raissi, M., Perdikaris, P., & Karniadakis, G. E. (2019). Physics-informed neural networks: A deep learning framework for solving forward and inverse problems involving nonlinear partial differential equations. *Journal of Computational Physics*, 378, 686–707. <https://doi.org/10.1016/J.JCP.2018.10.045>
- Rodriguez-Torrado, R., Ruiz, P., Cueto-Felgueroso, L., Green, M. C., Friesen, T., Matringe, S., & Togelius, J. (2022). Physics-informed attention-based neural network for hyperbolic partial differential equations: application to the Buckley–Leverett problem. *Scientific Reports 2022 12:1*, 12(1), 1–12. <https://doi.org/10.1038/s41598-022-11058-2>
- Schmid, K. S., & Geiger, S. (2012). Universal scaling of spontaneous imbibition for water-wet systems. *Water Resources Research*, 48(3), 1–16. <https://doi.org/10.1029/2011WR011566>
- Wang, S., Wang, H., & Perdikaris, P. (2021). On the eigenvector bias of Fourier feature networks: From

regression to solving multi-scale PDEs with physics-informed neural networks. *Computer Methods in Applied Mechanics and Engineering*, 384, 113938.

Wang, S., Yu, X., & Perdikaris, P. (2022). When and why PINNs fail to train: A neural tangent kernel perspective. *Journal of Computational Physics*, 449, 110768. <https://doi.org/10.1016/J.JCP.2021.110768>

Wu, C., Zhu, M., Tan, Q., Kartha, Y., & Lu, L. (2023). A comprehensive study of non-adaptive and residual-based adaptive sampling for physics-informed neural networks. *Computer Methods in Applied Mechanics and Engineering*, 403, 115671. <https://doi.org/10.1016/J.CMA.2022.115671>

Appendix A: Derivation of The Scaled Representation

The derivation of the scaled system Eqs. 5 and 6 from Eqs. 3 and 4 follows the steps from (Andersen, 2023b), as outlined briefly below. The variables related to the spatial axis, time, saturation, and capillary pressure are scaled as:

$$X = \frac{x}{L}, \quad T = \frac{t}{\tau}, \quad S_n = \frac{s_w - s_{wr}}{s_w^{eq} - s_{wr}}, \quad S = \frac{s_w - s_{wr}}{\Delta s_w}, \quad P_c = \sigma \sqrt{\frac{\phi}{K}} J \quad A1$$

where $\Delta s_w = 1 - s_{or} - s_{wr}$ is the mobile water saturation range. $J(S)$ is the J-function and represents a scaled capillary pressure curve. S is a scaled saturation covering mobile saturations and is used to define the relative permeabilities and J-function. The time scale τ is represented by:

$$\tau = \frac{\mu_m \Delta s_w L^2}{\sigma \sqrt{k/\phi \bar{\Lambda}}} \quad A2$$

where $\Lambda(S_n)$ is a diffusion coefficient function defined as:

$$\Lambda = \frac{k_{rw} k_{ro} \left(-\frac{dJ}{dS}\right)}{\left(\frac{\mu_o}{\mu_w}\right)^{0.5} k_{rw} + \left(\frac{\mu_w}{\mu_o}\right)^{0.5} k_{ro}} \quad A3$$

and $\bar{\Lambda}$ is its average value over the imbibing saturation interval:

$$\bar{\Lambda} = \int_{S_n=0}^1 \Lambda(S_n) dS_n \quad A4$$

The normalized function $\Lambda_n(S_n)$ is then defined as:

$$\Lambda_n(S_n) = \frac{\Lambda(S_n)}{\bar{\Lambda}}, \quad A5$$

Appendix B: Results of PINN Training

In this appendix, the full details of the PINN results for both cases A and B are summarized in Table A1. Also, the correlation between the value of the defined loss term and the MAE of the saturation (parameter of interest) is shown in Figure A1.

Table A1: A summary of PINN errors for cases A and B and different formulations. The results are shown for both ET and FT. The terms \mathcal{F} and \mathcal{B}_2 in different formulations are not on the same scale, thus not directly comparable (definitions are provided in Eqs. 13-22).

Case	PDE	Time Period	MAE			Loss terms (MAE)			
			S_n	P_c (bar)	RF	\mathcal{F}	\mathcal{J}	\mathcal{B}_1	\mathcal{B}_2
A	XT	ET	0.035	0.033	0.012	0.154	4.4e-02	4.1e-01	1.3e-02
		LT	0.015	0.001	0.003	0.028	4.4e-02	7.8e-02	1.6e-02
		FT	0.019	0.007	0.001	0.054	4.4e-02	1.5e-01	1.5e-02
	XY	ET	0.021	0.025	0.013	1.209	3.3e-02	2.9e-01	2.1e-02
		LT	0.005	0.001	0.001	0.090	3.3e-02	4.6e-02	1.4e-02
		FT	0.009	0.006	0.003	0.324	3.3e-02	9.8e-02	1.5e-02
	Z	ET	0.010	0.008	0.002	7.731	6.1e-04	8.2e-04	2.2e-03
B	XT	ET	0.027	0.019	0.007	1.72	3.4e-02	1.5e-01	1.2e-02
		LT	0.013	0.002	0.008	0.05	3.4e-02	3.3e-02	1.8e-02
		FT	0.021	0.008	0.013	0.424	3.6e-02	7.1e-02	9.1e-03
	XY	ET	0.020	0.016	0.007	1.08	2.6e-02	1.1e-01	1.3e-02
		LT	0.006	0.001	0.001	0.05	2.6e-02	3.0e-02	8.4e-03
		FT	0.009	0.005	0.003	0.33	2.6e-02	5.5e-02	9.7e-03
	Z	ET	0.016	0.014	0.013	26.411	8.3e-04	6.3e-03	9.7e-03

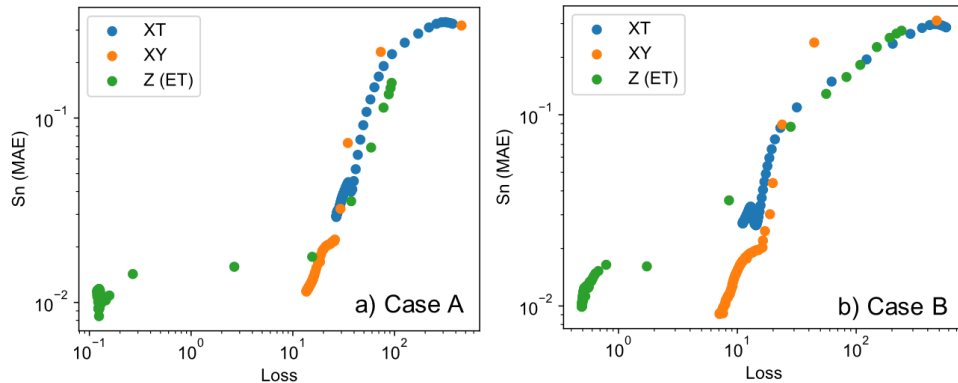


Figure A1: The correlation between the defined loss term and the MAE in the saturation profile, a) case A, b) case B.

Appendix C: Visualization of Loss Landscapes

To visualize the loss landscape of different PINN models, considering the high-dimensional non-convex loss functions we normally deal with, we used the approach introduced by Li et al. (2018). In this approach, a weighted interpolation between the trained model parameters, i.e., $\theta^* = \{w^*, b^*\}$ and two random model parameters, i.e., θ^1 and θ^2 is carried out, as:

$$f(\alpha_1, \alpha_2) = \mathcal{L}_S(\theta^* + \alpha_1\theta^1 + \alpha_2\theta^2) \quad 26$$

Where α_1 and α_2 are direction vectors that is varied in the range of 0 to 1. Also, \mathcal{L}_S represents the MAE of the saturation compared to the true values. We used a resolution of 100 points for each α_1 and α_2 vectors (in total, 10000 points) to have a clear view of the loss landscape. θ^1 and θ^2 are neural networks with exactly same architecture as the trained PINN network (θ^*) but with randomly initialized weights and biases. After regenerating the network at each point, the model is evaluated in the spatial and

temporal range introduced previously (Case A), and the MAE values of the predicted saturation were calculated.

Appendix D: Sampling Schemes

Sampling Scheme for Temporal Variables

Proper sampling of the collocation points in the spatiotemporal dimensions is an essential component in efficiently solving PDEs using PINNs, as previously reported (Daw et al., 2022; Nabian et al., 2021; Wu et al., 2023). In this section, we analyze the impact of different sampling strategies of temporal collocation points on the accuracy of the PINN solutions. Firstly, we chose $n_x = 100$ with uniform distances. In the temporal dimension, we tried five different number of points $n_t = \{5, 10, 20, 30, 40\}$, using two different schemes: constant DT , and constant DY . All the models were trained in the same x and t ranges. The time conversion between the different schemes was carried out using $Y = T^{0.5}$ as described in previous sections.

Table A2 summarizes the MAE of the PINNs solutions in the tested sampling strategies. The constant DY sampling approach performed better than constant DT for both XT and XY formulations. Increasing n_t rarely had impact (in the investigated range) when a constant DT was used, then higher numbers of n_t are needed to achieve acceptable MAEs. With constant DY , only $n_t=30$ for XY and $n_t=10$ for XY formulations were needed. The possible reason behind the results is that the DT based sampling tends to focus more on higher times, and more temporal points are needed to capture the details at low times. The constant DY sampling approach is more compatible with the nature of COUCSI, where there is a constant production rate versus Y in the ET period. This means the $\partial RF/\partial Y$ would be steadier than $\partial RF/\partial T$, making it easier to train the PINN model based on the whole imbibition period.

The main conclusion from these investigations is that using a constant DY is more efficient than a constant DT when selecting temporal collocation points for training the PINN, regardless of whether XT or XY formulations are used.

Table A2: Saturation MAE for different sampling approaches as a function of the number of temporal collocation points. All the simulations were performed for case B and at the same time ranges.

Formulation	Sampling Strategy	Number of Temporal Points (n_t)				
		5	10	20	30	40
XT	DT	13.52	11.14	9.08	9.42	9.12
	DY	13.25	12.82	6.92	1.82	1.50
XY	DT	7.94	5.47	7.05	8.01	8.21
	DY	8.22	1.37	1.24	1.23	1.27

Required Number of Collocation Points

Next, we consider how many collocation points are necessary to train the different PINN formulations. Based on the findings of the previous section, fewer temporal points can be used when using a constant DY approach. For case B, PINNs were trained for the FT period in XT and XY formulations and for ET with Z formulation. We investigated the PINN performance from the variation of n_t and n_x values ranging from very low to large. The results are shown in Figure A2: .

Figure A2a shows that for the XT formulation, n_t needed to be at least 40 for the MAE to stabilize, while for the XY formulation $n_t = 10$ was enough. On the other hand, in the Z formulation (in the ET period), the lowest error was achieved when $n_t = 1$, and when we increased n_t , the error slowly increased. At a given number of n_t the error was higher for XT than for XY , which again was higher than for Z

formulation. The increasing error of the Z formulation may be related to a more significant fraction of the collocation points containing trivial data (where the solution at the given point is at initial saturation). Using only one temporal point with Z formulation is possible since the solution depends on only one variable. By selecting a time where the Z-range does not span much further than the early time solution front, more non-trivial data points will be among the spatial collocation points.

Figure A2b shows the sensitivity of PINN performance to the n_x values. The XT performance stabilized for $n_x > 20$, while for XY it needed higher spatial points. For the Z formulation, only 30 points were needed. Overall, we can state that the XT formulation needs higher number of collocation points (especially temporal) compared to the XY (and Z) formulation, and regardless obtains higher error.

Figure A3 compares saturation profiles vs. Z with the different formulations at ET using $n_x = \{10, 30, 100\}$ to see the impact of the number of spatial collocation points. The FD solution (blue) is provided as a reference. In all cases, the PINN solution converges toward the FD solution by increasing n_x . With the Z formulation the solution overlaps exactly at $n_x \geq 30$ except at the lowest saturations. Increasing n_x significantly impacted the XY formulation from $n_x = 10$ to $n_x = 80$ by collecting the curves more closely to each other and to the FD solution. The curves at far from the earliest times are closest to the FD solution and overlap well with each other, while the curves at earliest times deviate more from the group. We should ideally not see any deviation between the curves until exactly when the closed boundary has been encountered. More collocation points appear to be needed to better collect the curves. For the XT and XY formulations, the solutions at low times are less accurate and deviate from the remaining curves as more flat and linear.

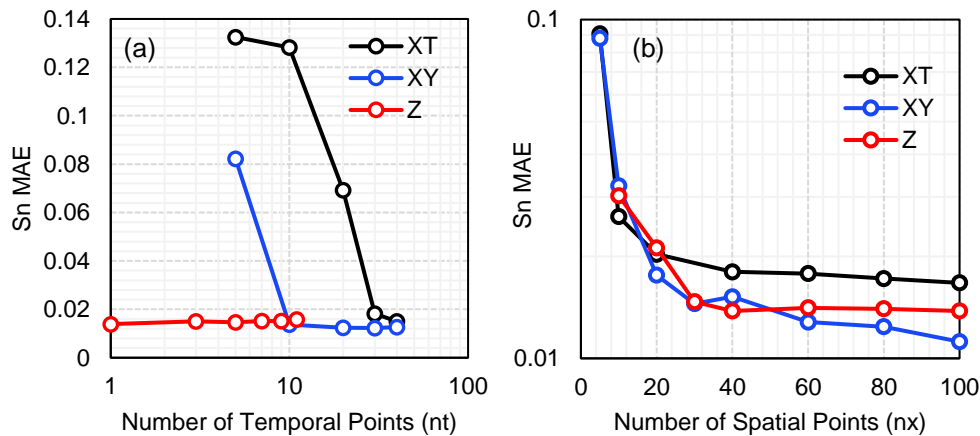


Figure A2: A sensitivity analysis of how the number of collocation points affects the PINN solutions for different formulations (case B). MAE in S_n vs: a) number temporal points (n_t) while $n_x = 100$, b) number spatial points (n_x), while $n_t = 30$ for XT and XY formulations, and $n_t = 1$ for Z formulation.

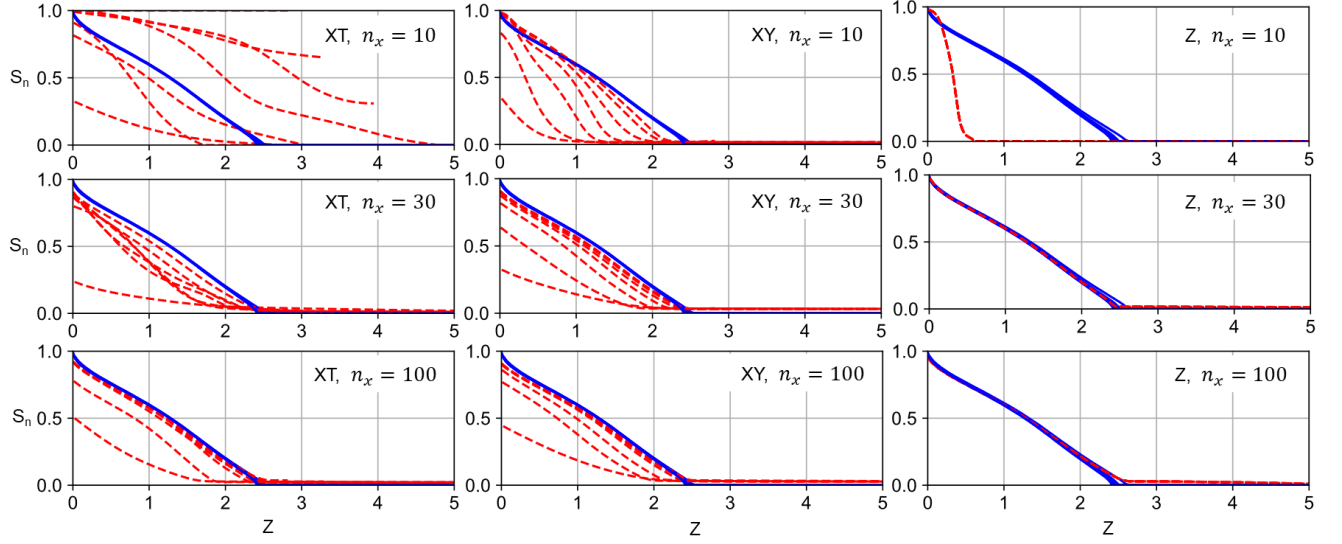
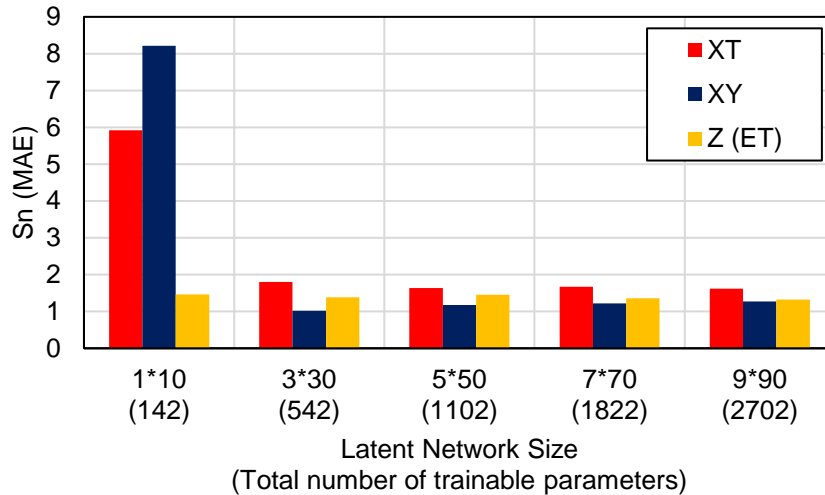


Figure A3: A sensitivity analysis of how n_x (the number of spatial collocation points) impacts the PINN saturation profiles for the different formulations (case B). S_n vs. Z is shown for $n_x = \{5, 20, 80\}$. All the figures correspond to the ET period. The blue line shows the FD solution, and the red lines show the PINN solutions. $n_t = 35$ for XT and XY formulations, and $n_t = 1$ for Z formulation.

Appendix E: Network Size

In this section, we investigate the performance of PINNs with different PDE formulations in different network complexities by changing the network size. We did it by varying the number of layers in the latent network. The depth of the decoder/encoder networks did not alter, although their width was kept identical to the width of the latent layer, which was varied. We did the investigations with $n_x = 100$ and $n_t = 35$ for all cases. The temporal collocation points were selected based on the constant DY sampling scheme.

The results for five different network sizes can be found in Figure A4. The network size could be reduced from having 2702 tuning parameters to 542 without significantly affecting the error in the XT and XY formulations, but further reduction had a noticeable effect. However, the Z formulation had a stable, good performance for all the network sizes with less error than the alternative formulations. It can be concluded that utilizing the more straightforward PDE formulation (e.g., shift from XT to Z formulation) is also helpful in reducing the required network complexity.



*Figure A4: The saturation MAE for different PINN network sizes. All the solutions are obtained based on the constant DY sampling strategy. The errors have been reported after 3000 epochs. The latent network size represents the depth*width of the network, while the number of trainable parameters also includes the encoder and decoder layers.*

Appendix F: Computational Costs

This section presents a comparison between the run-time of PINN and FD-based numerical simulation. The PINN model was implemented using Python and as a benchmark to ensure a fair comparison, we employed the MATLAB Reservoir Simulation Toolbox (MRST) (Krogstad et al., 2015), which utilizes optimized and computationally efficient solvers. The MRST solutions were obtained by utilizing a fully implicit two-phase (liquid-liquid) black-oil solver that utilizes an automatic differentiation-based gradient calculation approach. The PINN calculations were implemented in Python 3.9.7 environment on top of PyTorch 1.13.

All the operations were performed on a laptop with an 11th Gen Intel(R) Core (TM) i9-11950H @ 2.60GHz CPU and 32 GB RAM and NVIDIA RTX A2000 GPU. The computations in both Python and MATLAB environments were performed on the CPU.

Figure A5 (a and b) presents a comparison of the solution-time of PINN for different PDE formulations for both cases A and B. According to the figure, the solution times for the XY and Z formulations were almost identical, taking approximately 30 seconds to reach the solution plateau. In contrast, the XT-based solutions took nearly 100 seconds to reach a similar plateau, indicating significantly higher run-times compared to the XY and Z formulations.

Figure A5 c compares the run-time of MRST to the PINN run-time before reaching the S_n MAE values of 0.03, 0.02, and 0.017. To account for the impact of random initialization of PINN (which impacts the trajectories on the loss-landscape), we calculated the PINN run-times based on the average of five similar runs. We represented the corresponding standard deviations at each point using shaded areas. The values were reported for six different spatial points (i.e., number of collocation points in PINN and number of cells in numerical simulation), $n_x = \{100, 200, 300, 400, 500, 600\}$.

According to the figure, the PINN solution reaches the MAE=0.03 approximation level faster than MRST, although obtaining lower errors requires more time. Furthermore, the PINN run-time for the quick approximation (MAE=0.03) was barely affected by the random initialization of the network, which highlights the reliability of PINN solutions. Figure A5 d illustrates how the choice of the number of temporal points affects the run-time for different MAE levels. The figure indicates that the run-time for

MAE=0.03 is minimally impacted by the number of temporal points, whereas lower error levels exhibit greater impacts, with the minimum run-time occurring at approximately 45 temporal points.

This observation provides insights into the computational efficiency of using PINNs for forward problems, at least for the 1D COUCSI problem. This suggests that PINN can provide a quick approximation for forward problems with lower computational costs than traditional numerical simulations. However, if a more accurate solution is required, the run-time of PINN could increase and become comparable to or even higher than that of MRST. Therefore, the choice between the two methods depends on the specific requirements of the problem at hand, and the desired level of accuracy.

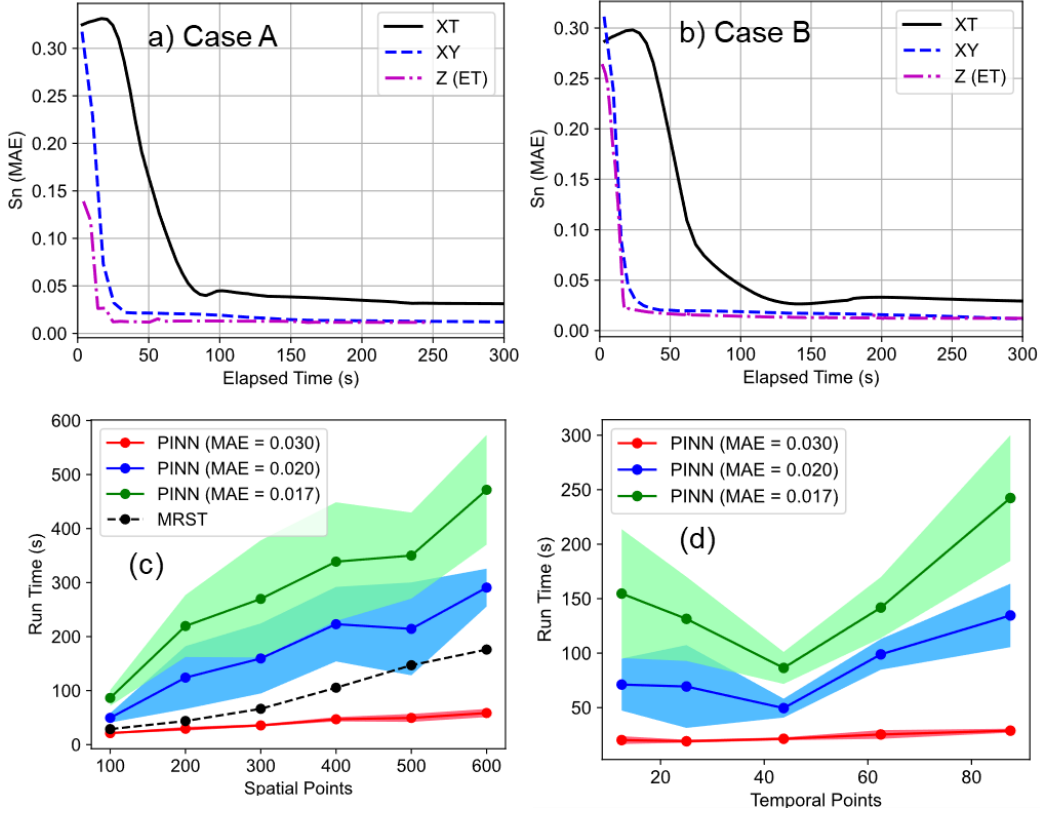


Figure A5: The run-time of PINN and its comparison to the numerical simulation (MRST). a) Comparing the solution time of PINNs for the different formulations, b) Run-time of PINN for reaching the Sn MAE values of 0.030, 0.020, and 0.017, compared to the run-time of MRST. c) Comparing the sensitivity of PINN and MRST to increasing the number of spatial points. d) Run-time of PINN for reaching the Sn MAE values of 0.030, 0.020, and 0.017 with a different number of spatial points.